



Weak gravitational lensing measurements of Abell 2744 using *JWST* and shear measurement algorithm `pyRRG-JWST`

David R. Harvey ¹★ and Richard Massey ²

¹Laboratoire d'Astrophysique, École Polytechnique Fédérale de Lausanne (EPFL), Observatoire de Sauverny, CH-1290 Versoix, Switzerland

²Centre for Extragalactic Astronomy, Department of Physics, Durham University, South Road, Durham DH1 3LE, UK

Accepted 2024 January 29. Received 2024 January 26; in original form 2023 December 21

ABSTRACT

We update the publicly available weak lensing shear measurement algorithm `pyRRG` for the *JWST*, and apply it to UNCOVER DR1 imaging of galaxy cluster Abell 2744. At short wavelengths ($<2.5\ \mu\text{m}$), shear measurements are consistent between independent observations through different *JWST* bandpasses, and calibrated within 1.5 per cent of those from the *Hubble Space Telescope*. At longer wavelengths, shear is underestimated by ~ 5 per cent, probably due to coarser pixellization. We model the spatially varying point spread function using `WebbPSF`, whose moments are within 0.05 of real stars near the centre of the mosaic, where there are sufficient stars to also generate an empirical model. We measure shear from up to 162 galaxies arcmin^{-2} to derive a map of dark plus baryonic mass with 12 arcsec (55 kpc) spatial resolution. All code, catalogues, and maps are available from <https://github.com/davidharvey1986/pyRRG>.

Key words: gravitational lensing: weak – galaxies: clusters: general – dark matter.

1 INTRODUCTION

Galaxy clusters are the largest known bound structures in our Universe, containing massive red elliptical galaxies and hot ionized gas, but dominated by a much more massive cocoon of dark matter; they have proved to be ideal laboratories to study the properties of dark matter (e.g. Clowe, Gonzalez & Markevitch 2004; Jee et al. 2005, 2012; Clowe et al. 2012; Harvey et al. 2015; Meneghetti et al. 2020; Bahé 2021; Sagunski et al. 2021; Meneghetti et al. 2023). Although dark matter seems not to interact with photons, so cannot be seen directly, it can be detected via gravitational lensing, the deflection of light from distant sources (see reviews Massey, Kitching & Richard 2010; Umetsu 2020). Gravitational lensing also magnifies the images of galaxies behind the cluster, presenting an opportunity to study the distant Universe at high resolution (e.g. Furtak et al. 2021; Bouwens et al. 2022; Atek et al. 2023).

Giant arcs produced by strong gravitational lensing were first properly resolved by the *Hubble Space Telescope* (*HST*). The *JWST* offers similarly transformative increases in imaging resolution and depth. In particular, weak gravitational lensing is the coherent distortion to the images of distant galaxies, whose light passes through the cluster on adjacent lines of sight. It is possible to measure the distorted shapes of these galaxies, but the dominant source of noise is the intrinsic variety of their shapes. If these are random, and with the empirical observation that the dispersion of their ellipticity is $\sigma_\gamma \approx 0.3$ (Leauthaud et al. 2007) we can achieve weak lensing signal-to-noise ratio ~ 1 along a typical line of sight near a cluster by averaging the shapes of ~ 50 galaxies. The resolution with

which dark matter can be mapped is thus limited by the density of resolved distant galaxies. The resolution and depth of *JWST* imaging reveals a higher density of galaxies than ever before seen (cf. Finner et al. 2023). This should allow us to detect subtle changes in the distribution and dynamics of dark matter predicted by alternative particle models of dark matter (e.g. Peter et al. 2013; Robertson et al. 2019; Banerjee et al. 2020).

As an example of the power of *JWST* we shall measure weak gravitational lensing by one of the most massive known galaxy clusters, Abell 2744 (A2744, at RA $00^{\text{h}}14^{\text{m}}20^{\text{s}}$, Dec. $-30^{\circ}23'19''$, redshift $z = 0.308$). This is an ongoing merger between several components, each of mass $>10^{14}M_\odot$. It has been well studied, but not all those studies agree, even about the relative masses of components – and the merger history that led to the observed configuration of galaxies, gas, and dark matter is complex (Merten et al. 2011). The cluster was first studied as one among a large sample of clusters, to investigate the observed discrepancy between X-ray masses and gravitational lensing masses (Allen 1998). In the first dedicated analysis, Merten et al. (2011, hereafter **M11**) used *HST* imaging to find strong lensing (Zitrin et al. 2010), then combined it with measurements of weak lensing to derive a ‘non-parametric’ (adaptive pixel grid) mass map. Medezinski et al. (2016, hereafter **M16**) used imaging from the Subaru telescope to construct a ‘non-parametric’ (pixellated) mass map using weak lensing but over a wider area. Abell 2744 was then selected as part of the Hubble Frontier Fields deep imaging survey, and a broad collaboration across the lensing community produced some of the highest resolution strong and weak lensing mass maps with Hubble (Lotz et al. 2017). Jauzac et al. (2016, hereafter **J16**) and Mahler et al. (2018) found significantly higher masses in all regions of the cluster, using the strong and weak lensing algorithm `Lenstool` (Jullo et al. 2007). Sebesta et al. (2019)

* E-mail: david.harvey@epfl.ch

Table 1. Overview of the *JWST* UNCOVER survey data (Bezanson et al. 2022), including data reduction parameters relevant to weak lensing measurements: the filter, the final pixel scale, the ‘drizzle’ kernel and ‘pixel fraction’ used to resample and stack multiple exposures, and the total exposure time in kiloseconds.

Filter	PixScale	Kernel	PixFrac	ET (ks)
<i>f115w</i>	0.02 arcsec	square	0.75	582.02
<i>f150w</i>	0.02 arcsec	square	0.75	467.87
<i>f200w</i>	0.02 arcsec	square	0.75	341.77
<i>f277w</i>	0.04 arcsec	square	0.75	83.77
<i>f356w</i>	0.04 arcsec	square	0.75	85.01
<i>f410m</i>	0.04 arcsec	square	0.75	53.60
<i>f444w</i>	0.04 arcsec	square	0.75	182.18

again used both strong and weak lensing, and used a different non-parametric mass mapping technique, showing that the assumption that light traces mass (assumed by parametric methods) holds. The recent acquisition of *JWST* imaging has led to the publication of several more strong lensing analyses (Bergamini et al. 2023a, b; Furtak et al. 2023; Cha et al. 2024, and this paper). Here we shall attempt to reconcile the apparent discrepancies between groups of these independent analyses.

Most importantly, we release open-source code `pyRRG-JWST` to measure the weak lensing signal and reconstruct the distribution of mass in any future *JWST* NIRCcam data. We use this opportunity to test for systematic or calibration biases in the method, and understand how uncertainty in *JWST*’s point spread function (PSF) affects measurements of shear.

2 WEAK LENSING THEORY

Weak gravitational lensing is the apparent distortion of a spatially extended background source of light by foreground matter. Following the notation of Narayan & Bartelmann (1996), if the distribution of foreground matter is thin compared to the distance to the source, its three-dimensional Newtonian potential, Φ , can be considered in two-dimensional projection:

$$\Psi = \frac{D_{LS}}{D_{LO}D_{SO}} \frac{2}{c^2} \int \Phi(x, y, z) dz, \quad (1)$$

where D is the angular diameter distance between the lens (L), source (S), and observer (O). Such a distribution of mass deflects passing rays of light by angle $\hat{\alpha}$, where the reduced deflection angle

$$\alpha = \frac{D_{LS}}{D_{SO}} \hat{\alpha} = \nabla \Psi. \quad (2)$$

Resolved background galaxies appear distorted if light from one side is deflected more than light at the other side. This is created by non-zero second derivatives of the potential

$$\kappa = \frac{1}{2}(\Psi_{11} + \Psi_{22}), \gamma_1 = \frac{1}{2}(\Psi_{11} - \Psi_{22}), \text{ and } \gamma_2 = \Psi_{12} = \Psi_{21}, \quad (3)$$

where convergence κ is an isotropic magnification, and shear γ_1 (γ_2) is an elongation in the east–west (north–west–south–east) direction.

From measurements of shear γ_i it is possible to calculate the convergence via either Bayesian inference to fit parametric models (e.g. Jullo et al. 2007) or directly via Fourier space (Kaiser & Squires 1993). The Fourier space inversion exploits the fact that both shear and convergence are derivatives of the same lensing potential so, following equation (3),

$$\tilde{\gamma}_i = \left[\begin{array}{c} (k_1^2 - k_2^2)/k^2 \\ 2k_2k_1/k^2 \end{array} \right] \tilde{\kappa}, \quad (4)$$

where tildes denote Fourier transforms, k is the wavenumber, and a complex field is obtained for convergence $\kappa = \kappa_E + i\kappa_B$, such that $\kappa_E = \kappa$ and κ_B should be zero in the absence of systematic bias.

Finally, we calculate the projected surface mass density:

$$\Sigma = \left[\frac{c^2}{4\pi G} \frac{D_{SO}}{D_{LS}D_{LO}} \right] \kappa. \quad (5)$$

Notice how the pre-factor depends only on the geometrical configuration of the lens and source. Throughout this paper, we shall assume a Planck cosmology (Planck Collaboration 2021) to convert between κ and mass.

3 DATA

We analyse reduced and stacked NIRCcam imaging from DR1 of the *JWST* UNCOVER survey,¹ a ~ 29 arcmin² mosaic near RA 00^h20^m00^s, Dec. $-30^\circ 22' 30''$ (see fig. 2 of Bezanson et al. 2022). We attempt to measure the weak lensing signal independently in all available bands (*f115w*, *f150w*, *f200w*, *f277w*, *f356w*, and *f444w*) to understand the behaviour of each (we do not include *f090w* since it does not have the same coverage as other bands). Parameters of the data relevant to weak lensing are summarized in Table 1.

4 SHEAR MEASUREMENT METHOD

To measure weak lensing shear from galaxies in the A2744 field, we adapt the publicly available code `pyRRG` (Rhodes, Refregier & Groth 2000; Leauthaud et al. 2007; Harvey et al. 2021) to the specifics of *JWST* NIRCcam data. This method is similar to the well-known KSB (Kaiser, Squires & Broadhurst 1995) method, but corrects all moments of a galaxy’s shape for convolution with the PSF before calculating an ellipticity, e_i^{obs} , from a ratio of its Gaussian-weighted quadrupole moments. Specifically the two components of uncorrected ellipticity, chi , of a galaxy is defined by

$$\chi_1 = \frac{J_{11} - J_{22}}{J_{11} + J_{22}} \chi_2 = \frac{2J_{12}}{J_{11} + J_{22}}, \quad (6)$$

where J_{xx} is the quadrupole, normalized weighted image moment.

Performing PSF correction first makes the calculation more stable in the presence of a diffraction-limited PSF whose extended wings mean that its moments converge slowly (note that Zhang, Luo & Foucaud 2015 propose an alternate solution to this problem). A local estimate of reduced shear can finally be obtained as $\tilde{\gamma}_i = e_i^{\text{obs}}/GC$, where shear responsivity G depends on the galaxy’s higher order moments:

$$G = 2 - \langle \chi^2 \rangle - \frac{1}{2} \langle \lambda \rangle - \frac{1}{2} \langle \chi \cdot \mu \rangle, \quad (7)$$

where $\langle \chi \cdot \mu \rangle = \chi_1\mu_1 + \chi_2\mu_2$, λ is a combination of the fourth-order image moments with

$$\lambda = (J_{1111} + 2J_{1122} + J_{2222})/(2d^2w^2), \quad (8)$$

where d is the size of galaxy, $d = \sqrt{0.5(J_{11} + J_{22})}$, w is a Gaussian weight function with a standard deviation of d , and the two components of μ are given by

$$\mu_1 = (-J_{1111} + J_{2222})/(2d^2w^2), \quad (9)$$

$$\mu_2 = -2(J_{1112} + J_{1222})/(2d^2w^2). \quad (10)$$

¹<https://jwst-uncover.github.io/DR1.html>

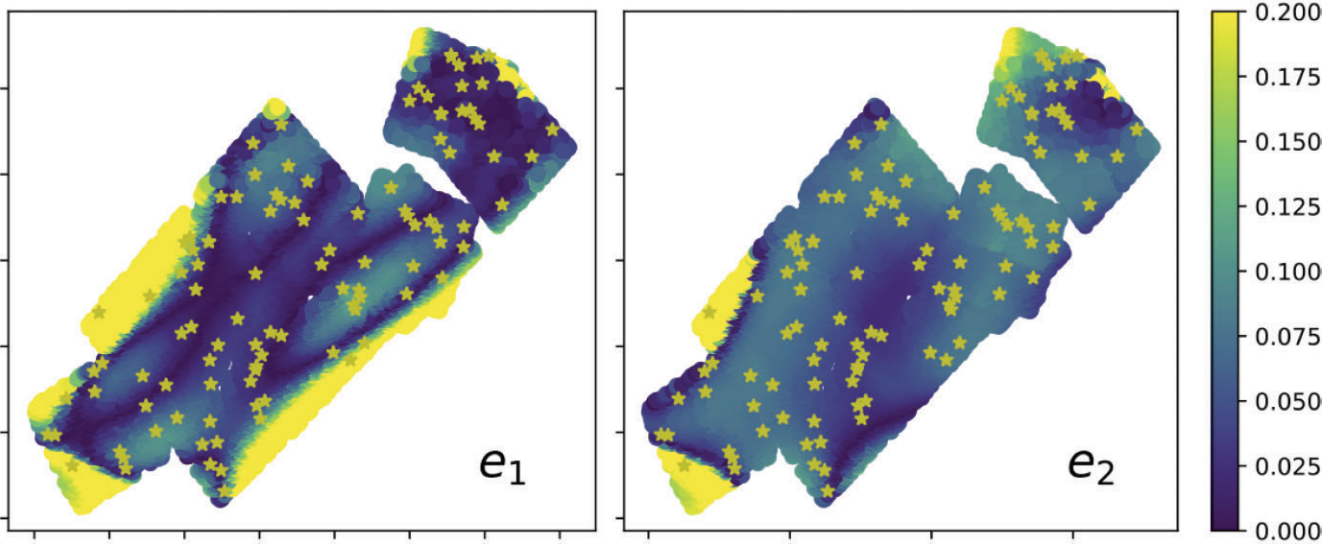


Figure 1. The difference between models of the spatially varying *JWST* PSF, calculated using *WebbPSF* or empirically interpolated from real, bright stars in the stacked image mosaic (shown as yellow stars). The left (right) panel shows absolute differences in the first (second) component of ellipticity. The models match near the centre of the mosaic, where real stars are plentiful, but the empirical model diverges at the edges, due to the low density of stars at galactic latitude -81° .

Table 2. Impact of various cuts in the catalogue to reach our final density of source galaxies for each filter given in units of galaxies per square arcminute. The first column shows the number density of objects in the initial source catalogue, followed by the number density of sources after star–galaxy separation and PSF correction, followed by the number density after size and magnitude cuts, then the removal of cluster members, then the drop due to matching to the photo-*z* catalogues then the final redshift cuts.

Filter	Initial Cat	PSF corrected	Size cuts	Cluster members	Median redshift
<i>f115w</i>	1670	1166	187	138.6	1.36
<i>f150w</i>	1864	1349	202	151.4	1.49
<i>f200w</i>	1877	1374	216	161.9	1.56

Finally $C = 0.86$ is a mean empirical calibration (Leauthaud et al. 2007). High et al. (2007) demonstrate that pixellization effects lead to different ideal values of C_1 for γ_1 and C_2 for γ_2 . However, There is no unique direction of pixellization in UNCOVER data, because the orientation of pixels is different in raw and stacked images. Moreover, since we are here interested only in non-local combinations of shear, the calibration averages over these two values: we have checked that neither our maps nor masses are changed within statistical significance by any combination of C_1 and C_2 such that $(C_1 + C_2)/2 = 0.86$.

4.1 Object detection

We find objects in the stacked images using *SEXTRACTOR* (Bertin & Arnouts 1996), with ‘hot’ and ‘cold’ runs to improve deblending (Leauthaud et al. 2007). We distinguish stars from galaxies using an interactive GUI to select loci in a space spanned by objects’ peak surface brightness μ_{\max} and integrated magnitude. We then measure the second and fourth Gaussian-weighted moments of every star and galaxy, with the Gaussian centred such that the first-order moment is zero (Rhodes, Refregier & Groth 2000).

4.2 Correction for the PSF

As we see above, we require both the second- and fourth-order moments in order to calculate the final shear. We thus must correct

the galaxies’ observed shape moments for convolution with for the *JWST* PSF, following section 5 of Rhodes, Refregier & Groth (2000). This requires estimates of the second- and fourth-order image moments of the PSF, interpolated to the location of every galaxy. Specifically we correct the second-order image moments J_{ij} of each galaxy via

$$J_{ij} = J'_{ij} - C'_{ijkl} P_{kl}, \quad (11)$$

where C' is convolution susceptibility tensor and is given by

$$C_{ijkl} = \delta_{ik}\delta_{jl} - \frac{2}{w^2} J_{ki}\delta_{jl} + \frac{1}{2w^4} [J_{ijkl} - J_{ij}J_{kl}], \quad (12)$$

and P is the unweighted PSF moments. Then the fourth-order image moments are given by

$$J_{ijkl} = J'_{ijkl} - P_{ijkl} - 6P_{ij}J'_{kl} + 6P_{ij}P_{kl}. \quad (13)$$

We can calculate the second- and fourth-order moments of the PSF throughout the image in two ways. The first is to empirically measure the moments of the stars at different points in the image and then interpolate to the position of the galaxies we want to correct. The second is to use a model of the *JWST* PSF at exactly the position of each galaxy. Unfortunately, at galactic latitude -81° , the UNCOVER images contain insufficient bright stars to do the first empirical method. We must therefore use a model and artificially plant stars in the *JWST* image, measure these

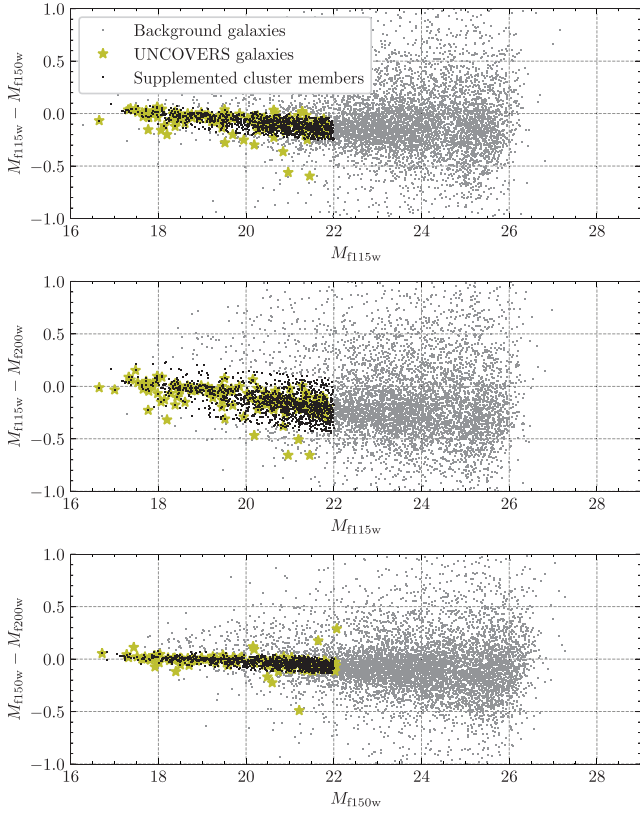


Figure 2. The shear catalogue excludes cluster member galaxies identified in combined *JWST*+*HST* photometry (yellow stars; Bezanson et al. 2022), but that covers only part of the *JWST* survey footprint. We use these to identify the cluster red sequence (bottom panel), and remove all galaxies in the red sequence throughout the survey.

moments, and use these as the PSF moments to correct the galaxies with.

To do this we first create a *JWST* NIRCcam image containing a dense grid of fake stars in each band, using the publicly available *WebbPSF*.² We measure the moments of these fake stars and fit a bivariate spline³ to interpolate to any point in the image. For the spline we use the default smoothing value recommended by *SCIPY*: the length of the input vector, which roughly equates to the standard deviation of the values (i.e. the error in the estimates of the moments). We also use a degree = 3 in each Cartesian direction. Then for each exposure that makes up the final drizzled image we calculate the moments for the PSF at the position of each galaxy, rotate it, and stack it across all exposures. This provides a model PSF at any point in the stacked image, accounting for rotations and discontinuities between exposures.

To validate the PSF, we also use splines to interpolate the observed moments of stars in the stacked image. This avoids reliance on *WebbPSF*, but does not account for discontinuities in the stacked image. Near the centre of the mosaic, when there are stars in every direction, the difference between real stars and the *WebbPSF* model is less than 0.05 in both components of ellipticity (Fig. 1). In the outskirts of the mosaic, the empirical interpolation struggles to

²<https://webbpsf.readthedocs.io/en/latest/index.html>

³<https://docs.scipy.org/doc/scipy/reference/generated/scipy.interpolate.RectBivariateSpline.html>

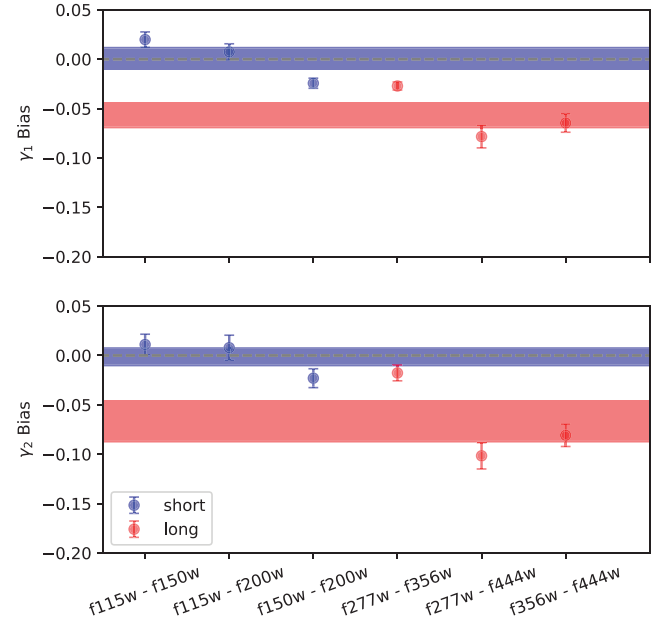


Figure 3. Internal consistency check and estimate of multiplicative bias in our shape measurements. For a fixed sample of galaxies, we measure shear independently in all the UNCOVER imaging bands. The top (bottom) panel shows the relative calibration in γ_1 (γ_2) between bands, assuming a linear scaling: zero would indicate statistically identical calibration. Error bars show 1σ uncertainties. The coloured regions show the average bias for various measurements at short (blue) and long (red) wavelengths. We find that the method has on average no significant bias in the short wavelengths and a ~ 5 per cent bias in the longer wavelengths.

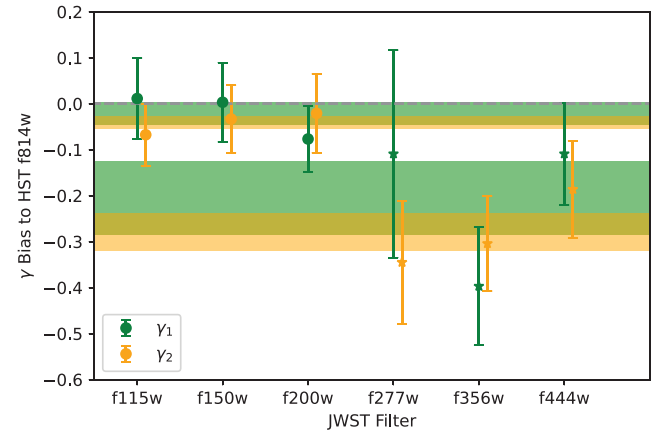


Figure 4. Shear measurement bias in measurements with *JWST*, relative to a matched sample of galaxies from *HST* F814W imaging of the same cluster (as measured by Harvey et al. 2015). The green (orange) points show the mean relative bias in measurements of γ_1 (γ_2). At short *JWST* wavelengths, the mean shear measurement bias is within typical requirements for cluster lensing science goals.

converge. None the less, we shall propagate these measurements through our full analysis, to quantify what difference they make to inferred cluster masses (cf. Finner et al. 2023), compared to the *WebbPSF* model.

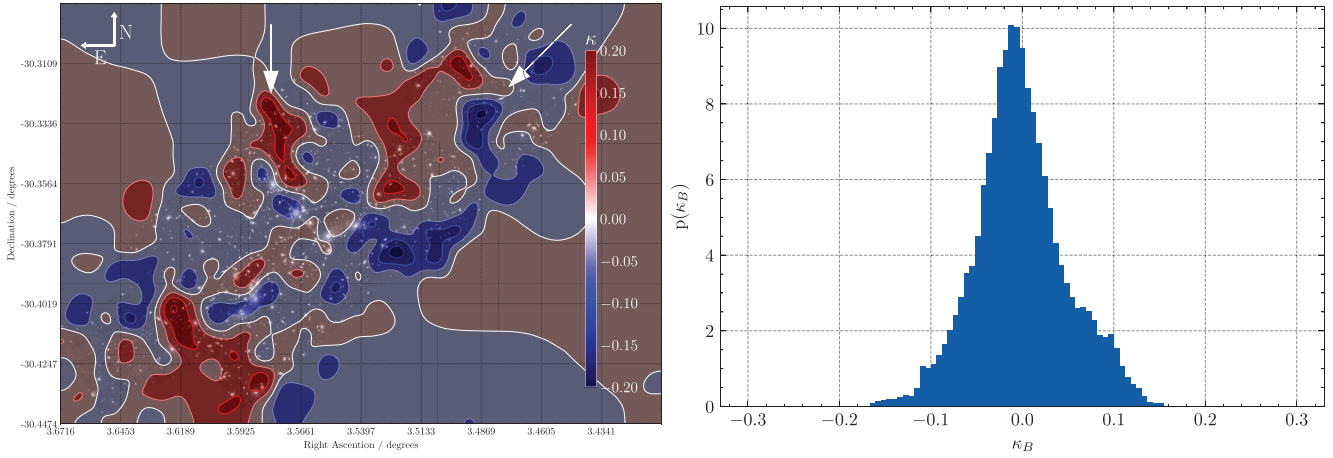


Figure 5. *Left:* Galaxy cluster Abell 2744 weak lensing B -mode convergence map, which should be consistent with zero in the absence of systematic errors. *Right:* A histogram of pixel values in the B -mode map shows a mean value consistent with zero, and standard deviation $\sigma_{\kappa} = 0.05$, which should therefore also indicate the level of statistical noise in the E -mode map.

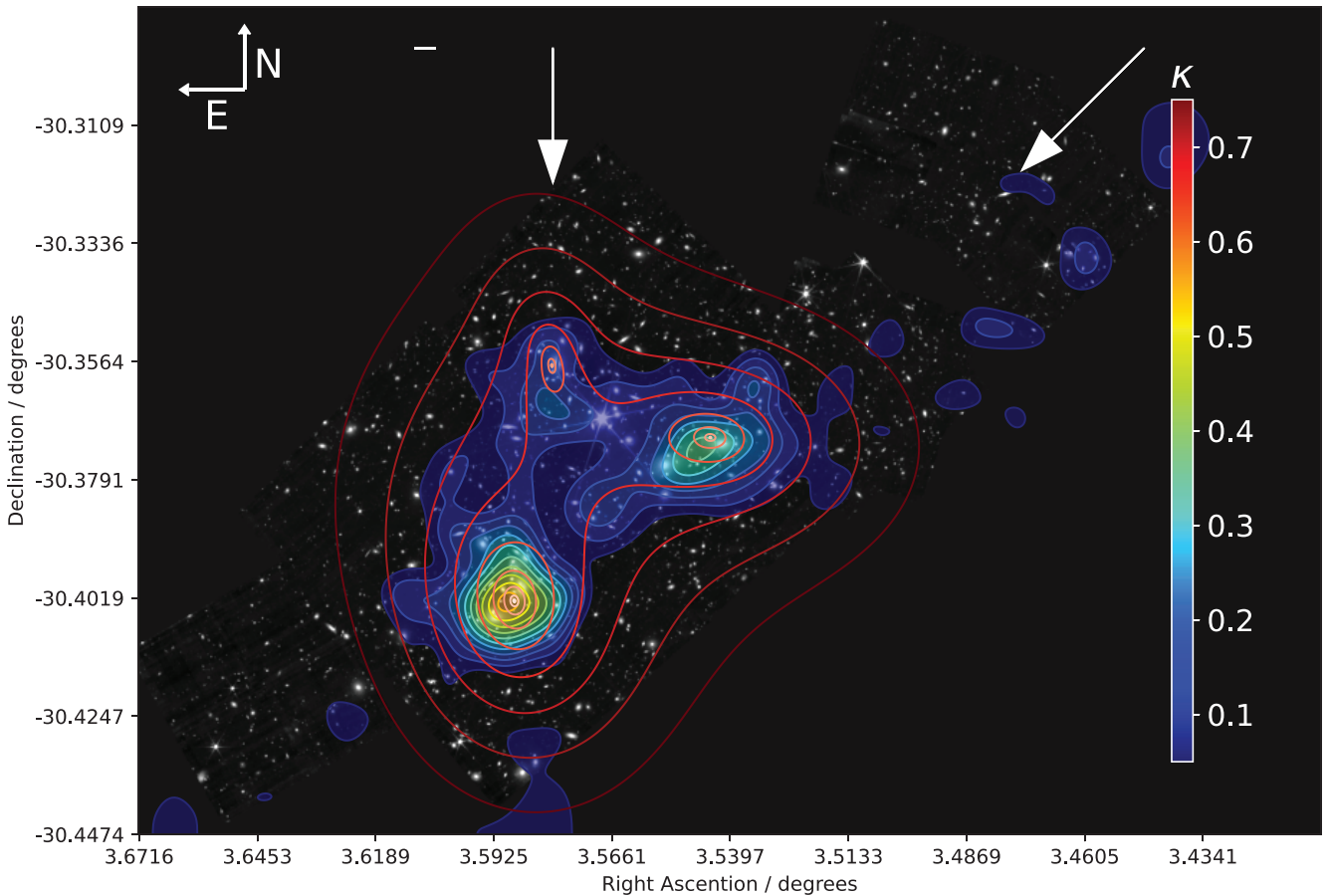
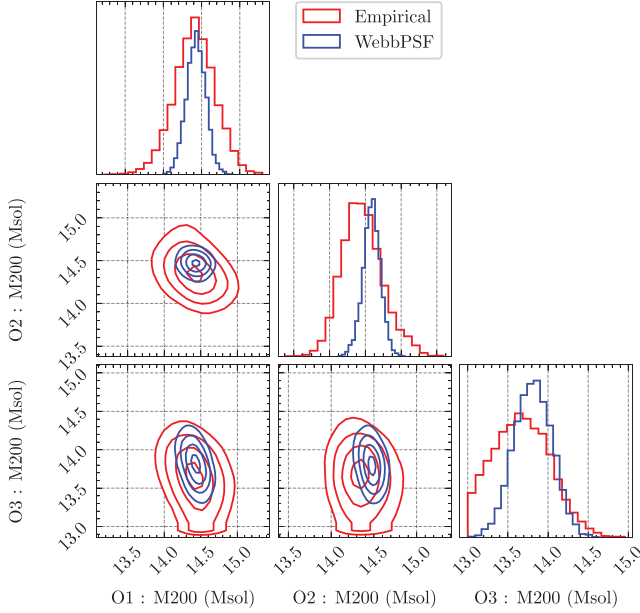


Figure 6. Galaxy cluster Abell 2744 in *JWST* band $f115w$, plus non-parametric map of weak lensing E -mode convergence, which is proportional to total mass. The lensing analysis combines shear catalogues from imaging in $f115w$, $f150w$, and $f200w$ bands, all of which reach an average density of 150 source galaxies arcmin $^{-2}$. The lensing data are binned in 12.8 arcsec pixels and smoothed by a Gaussian filter of FWHM 17 arcsec, which optimizes overall signal-to-noise ratio. The first isodensity contour is at $\kappa = 0.05$, with subsequent contours in steps of $\Delta\kappa = 0.05$. We also show the best-fitting *Lencool* model in red contours. The arrows in the north and north-west indicate the direction of filaments identified by Eckert et al. (2015).

Table 3. Results of the `Lenstool` fit to the combined filters, $f115w$, $f150w$, and $f200w$ using `WebbPSF` to model the PSF. The offsets are with respect to the reference point (3.556, -30.369).

Clump	x (arcsec)	y (arcsec)	Ellipticity e	Orientation θ (deg)	Concentration c	$\log(M_{200}/M_{\odot})$
Core	-293^{+2}_{-2}	$-225^{+3}_{-2.30}$	$0.17^{+0.06}_{-0.06}$	$91^{+9}_{-10.37}$	$3.4^{+0.7}_{-0.6}$	$14.5^{+0.1}_{-0.1}$
NW	-160^{+5}_{-3}	$-118^{+2}_{-2.54}$	$0.15^{+0.07}_{-0.06}$	$20^{+17}_{-11.26}$	$2.0^{+0.5}_{-0.4}$	$14.4^{+0.1}_{-0.1}$
N	-261^{+6}_{-4}	-70^{+7}_{-6}	$0.26^{+0.14}_{-0.13}$	$119^{+20.84}_{-22}$	$2.7^{+2.1}_{-1.2}$	$13.8^{+0.3}_{-0.2}$

**Figure 7.** Posterior probabilities for the M_{200} mass of the three structures identified in the A2744 field. The blue contours show measurements from shears corrected for the PSF using `WebbPSF`; red contours show measurements using an empirical PSF model interpolated from bright stars in the field.

4.3 Galaxy catalogue selection cuts

4.3.1 Size and brightness cuts

The RRG shear estimator (section 4.4 of Rhodes, Refregier & Groth 2000) is a ratio of shape moments measured for each galaxy. The cuts applied to catalogue of galaxy shapes sets a balance between reducing statistical noise by including more galaxies, versus growing systematic bias (Refregier et al. 2012) by including galaxies that are faint or small compared to the pixel scale. The optimum balance depends on the overall science goal, but for studies of individual clusters, we find a suitable compromise by a binary inclusion of galaxies with individual signal-to-noise ratio >4.4 (as explored empirically by Leauthaud et al. 2007). We also impose a radius cut of 4 pixels (~ 20 per cent larger than the PSF) and a minimum of three FWHM distance between adjacent galaxies in crowded fields. This results in a shear catalogue containing 145–168 galaxies arcmin^{-2} , depending on the band (Table 2).

4.3.2 Redshift cuts

Galaxies in (or in front of) the cluster will not be gravitationally lensed by it. Including them in any average shear measurement would spuriously dilute the shear signal and bias the inferred cluster mass.

To remove cluster member galaxies, we first note all galaxies in the Bezanson et al. (2022) catalogue (other publicly available catalogues are also available from Furtak et al. 2023 and Weaver et al. 2024). This is derived from *HST* imaging and does not completely cover the *JWST* field of view, so we supplement it using the known cluster members to identify the red sequence in each combination of short *JWST* wavelengths (Fig. 2). This sequence is tightest in the $f150w$ and $f200w$ bands since these bracket the Balmer break. We remove from our catalogue all galaxies within 1σ scatter of $|m_{f150w} - m_{f200w}| < 0.08$ of that fitted line.

To remove foreground galaxies, we also use UNCOVER photometry and photometric redshifts to identify all galaxies brighter than $m_{f150w} < 22$, or at redshift $z < 0.350$. The latter accounts for photometric redshift uncertainty, and also ensures that all galaxies have high lensing efficiency.

After cuts, the shear catalogues contain ~ 150 galaxies arcmin^{-2} in each band (see Table 2 for the exact number in each band and the impact of each cut), at median photometric redshift $z \sim 1.72$ (Bezanson et al. 2022).

4.4 Tests of shear calibration

4.4.1 Relative calibration between bands

We make independent measurements of galaxies' shear using every band of UNCOVER imaging. Since shear is independent of wavelength, shear estimators for a matched galaxy catalogue should be consistent with one another (they will not be identical because galaxies' intrinsic shapes e^{int} vary as a function of wavelength).

To compare shear measurements from two bands (say band A and band B), we use Orthogonal Distance Regression⁴ to fit $\gamma_i^B = (1 + m_i)\gamma_i^A + C_i$ (cf. Heymans et al. 2006; Massey et al. 2007b). Since imaging in different bands is drizzled to different pixel scales (see Table 1), we compare only shear measurements from similarly drizzled bands, i.e. short wavelengths with short wavelengths and long wavelengths with long wavelengths. We find consistent behaviour in each regime, so also calculated the average biases between all pairs of bands at adjacent wavelengths (see Fig. 3). At short wavelengths (where images have 0.02 arcsec pixels) there is no significant bias (between bands) with $m_1 = 0.0 \pm 0.01$ and $m_2 = 0.001 \pm 0.009$, 68 per cent confidence limit. At long wavelengths (where images have 0.04 arcsec pixels), the typical bias is $m_1 = -0.06 \pm 0.01$ and $m_2 = -0.07 \pm 0.02$, or less than 10 per cent at 68 per cent confidence limit. In all cases we find an additive bias consistent with zero.

⁴<https://docs.scipy.org/doc/scipy/reference/odr.html>

Table 4. Our results in the context of similar studies looking at A2744 with the probes (WL – weak lensing, SL – strong lensing) shown. We find that we underestimate the mass of the core with respect to **J16** and **M11** who both use strong lensing. However we are consistent with **M16** who uses Subaru data. Our estimate of the North-Western and Northern halo are consistent with **M11** however underestimated with respect to **J16**.

Clump	$M(<250 \text{ kpc}) / 10^{13} M_{\odot}$ This work (WL)	$M(<250 \text{ kpc}) / 10^{13} M_{\odot}$ Jauzac et al. (2016) (WL+SL)	$M(<250 \text{ kpc}) / 10^{13} M_{\odot}$ Merten et al. (2011) (WL+SL)	$M(<250 \text{ kpc}) / 10^{13} M_{\odot}$ Medezinski et al. (2016) (WL)
Core	$16.0^{+0.6}_{-0.9}$	27.7 ± 0.1	22.4 ± 5.5	14.9 ± 3.5
NW	$10.8^{+0.3}_{-1.0}$	18.0 ± 1.0	11.5 ± 2.3	7.6 ± 3.5
N	$6.5^{+0.7}_{-0.9}$	8.6 ± 2.2	–	–

4.4.2 Relative calibration with respect to HST

The pyRRG algorithm has been calibrated for *HST* observations in the $f814w$ band using mock imaging with known shear (Leauthaud et al. 2007) and subsequently used in many analyses of real data (e.g. Massey et al. 2007a; Merten et al. 2011; Harvey et al. 2015; Jauzac et al. 2016; Schrabback et al. 2018; Tam et al. 2020). We match *JWST* galaxies with those detected in *HST* imaging by Harvey et al. (2015), and compute the same linear fit as above (see Fig. 4). At shorter *JWST* wavelengths we find no significant bias m_1 , but $m_2 \approx 3$ per cent. A limitation of this approach is that only the brighter and bigger galaxies detected by *JWST* are also detected by *HST*. None the less, the measurements with these two different observatories is completely independent, so their consistency within these bounds is encouraging.

4.4.3 Interpretation

The pyRRG algorithm appears to meet most cluster science requirements in *JWST* bands at $<2.5 \mu\text{m}$. The main cause of bias at longer wavelengths is probably the larger pixels. RRG treats pixellation as a component of the PSF, which is mathematically accurate to only first order, and creates biases when pixels are coarse (High et al. 2007). This effect is already accounted for in the empirical calibration of RRG at short wavelengths and small pixels (Leauthaud et al. 2007).

5 RESULTS

5.1 Non-parametric mass map

We average shear measurements from $f115w$, $f150w$, and $f200w$ bands in a grid of 64×44 square pixels, each 12.8 arcsec on a side and containing a median of 20 galaxies. We assume the shear in each pixel is median redshift of every mean shear measurement is $z = 1.72$.

There is a statistical excess of galaxies near cluster cores, probably caused by interloper cluster members in our catalogue, even after the cuts intended to remove them (see Section 4.3.2). To account for their dilution of the shear signal, we also pixellate a map of galaxy number density n_{gal} and smooth it with a Gaussian of width $\sigma = 1$ pixel. We find that the median number of galaxies in each pixel is 11 and therefore in any pixel containing more than 11 galaxies, we multiply both components of $\tilde{\gamma}_i$ by $n_{\text{gal}}/11$. Even the most populated pixel contains only 18 galaxies, and this procedure does not change the map within statistical precision.

We convert the pixellated shear map into a pixellated convergence map using equation (4) (Kaiser & Squires 1993). Since the orientation of the data means that the map contains a lot of empty pixels around it already, we do not need to pad with additional zeros during the Fourier transforms. We then account for the discrete nature of the sampling of this field by smoothing the convergence map by convolving with a Gaussian of standard deviation 12 arcsec.

We find that this amount of smoothing suitably balances precision (retaining the signal) and accuracy (suppressing the noise). After smoothing, the imaginary component of reconstructed convergence, κ_B , is consistent with zero, as it should be in the absence of systematic biases, and its pixel values have standard deviation $\sigma_{\kappa_B} = 0.05$ (Fig. 5). This empirical measurement of statistical precision incorporates all sources of noise in the shear catalogue, and should also apply to the real component of convergence, κ_E .

The κ_E convergence field contains three peaks, which match previous identification as Core, North-West, and North substructures (Merten et al. 2011; Jauzac et al. 2016; Bergamini et al. 2023b; Furtak et al. 2023). Unfortunately the western halo found in previous studies lies just outside the UNCOVER survey footprint. The cluster member density and convergence trace each other extremely well, with filamentary extensions towards the north and north-west, corresponding to filaments identified by Eckert et al. (2015), and shown as arrows in Fig. 6.

5.2 Parametric mass reconstruction

To infer the mass of the three components using as much information as possible, we also fit a parametric model directly to the shear (and hence require no regularized grid) consisting of three (Navarro, Frenk & White 1997) profiles. This has 18 free parameters: each component has unknown mass M_{200} , position (x, y) , ellipticity (e, θ) , and concentration. We use relatively loose, flat priors on each position within ± 25 arcsec, the logarithm of halo mass between 10^{13} and $10^{16} M_{\odot}$, concentration between 0 and 20, ellipticity between 0 and 1, and orientation of the major axis between 0° and 180° .

To optimize the fit, we use the MCMC search inside `Lenstool` (Jullo et al. 2007). Rather than binned shears, this takes measurements of every galaxy’s shear and photometric redshift (which we extract from the UNCOVER catalogue; any galaxies without a photometric redshift we assume to be at $z = 1.72$). Note that we do not attempt to correct for shear dilution by superfluous cluster member galaxies in the catalogue.

The best-fitting model parameters have statistical uncertainty ~ 2 per cent (Table 3, with the posterior probability of cluster masses in Fig. 7). Reassuringly, these observable quantities are robust within statistical uncertainty, regardless of the method used to model the PSF, or if shears without photometric redshifts are instead excluded, except that the uncertainties broaden.

To compare our measurements to previous studies that state or for which it is possible to integrate the projected mass within a fixed radius, we similarly integrate our free-form mass map within 250 kpc of the best-fitting centres (Table 4). Our results are statistically consistent with **M16**, who used weak lensing measurements from Subaru imaging, and (in the North-Western and Northern structures) **M11**, who used weak and strong lensing measurements from *HST*. However, we measure a lower mass for the core than **M11**, where

there is a high density of strong lensing constraints, and lower masses for all three structures than J16, who use only strong lensing.

6 CONCLUSIONS

We use six-band *JWST*-NIRCam imaging from UNCOVER data release 1 to measure weak gravitational lensing by the merging cluster A2744. The unmatched resolution and depth of *JWST* imaging achieve unprecedented resolution in the mass map, from shear measurements of 170 galaxies arcmin⁻². However, consistent with previous studies, we identify three main mass components. The growing number of such independent analyses indicate that measurements from different telescopes are more consistent with each other than measurements using different (strong versus weak lensing) techniques. Our mass estimates are consistent with the weak lensing-only measurements of M16, but are lower than the combined strong and weak lensing measurements of M11 and J16. A similar dichotomy has been seen before in other clusters. Identifying the discrepancies between strong and weak lensing will require further work, but in this case may also be exacerbated by uncertainty and bias in the photometric redshifts of very faint *JWST* galaxies.

For this kind of individual cluster lensing analysis, we find that the pyRRG shear measurement method is sufficiently accurate to meet most science requirements. Measurements in bands at wavelengths <2.5 μm are consistent with each other and with measurements from *HST*: both comparisons indicate multiplicative shear measurement bias better than 2 per cent. The WebbPSF model produces arbitrarily dense grids of stars throughout a mosaiced image, whose ellipticities agree with real stars within $\Delta e < 0.05$. However, pyRRG shear measurements in bands at longer wavelengths are not reliable, with multiplicative biases up to ~ 10 per cent between bands and >30 per cent with respect to *HST*. This is likely because of the 0.04 arcsec pixels, which are larger than the 0.02 arcsec pixels used at shorter wavelengths.

We publicly release all shear measurement code and catalogues at <https://github.com/davidharvey1986/pyRRG>, for any future work using weak lensing with *JWST*.

ACKNOWLEDGEMENTS

This work was supported by the Swiss State Secretariat for Education, Research and Innovation (SERI) under contract number 521107294.

DATA AVAILABILITY

All code and data are publicly available at <https://github.com/davidharvey1986/pyRRG>

REFERENCES

Allen S. W., 1998, *MNRAS*, 296, 392
 Atek H. et al., 2023, *MNRAS*, 519, 1201
 Bahé Y. M., 2021, *MNRAS*, 505, 1458
 Banerjee A., Adhikari S., Dalal N., More S., Kravtsov A., 2020, *J. Cosmol. Astropart. Phys.*, 2020, 024
 Bergamini P. et al., 2023a, *A&A*, 670, A60
 Bergamini P. et al., 2023b, *ApJ*, 952, 84

Bertin E., Arnouts S., 1996, *A&AS*, 117, 393
 Bezanson R. et al., 2022, preprint (arXiv:2212.04026)
 Bouwens R. J., Illingworth G., Ellis R. S., Oesch P., Stefanon M., 2022, *ApJ*, 940, 55
 Cha S., HyeonHan K., Scofield Z. P., Joo H., Jee M. J., 2024, *ApJ*, 961, 186
 Clowe D., Gonzalez A., Markevitch M., 2004, *ApJ*, 604, 596
 Clowe D., Markevitch M., Bradač M., Gonzalez A. H., Chung S. M., Massey R., Zaritsky D., 2012, *ApJ*, 758, 128
 Eckert D. et al., 2015, *Nature*, 528, 105
 Finner K., Faisst A., Chary R.-R., Jee M. J., 2023, *ApJ*, 953, 102
 Furtak L. J., Atek H., Lehnert M. D., Chevallard J., Charlot S., 2021, *MNRAS*, 501, 1568
 Furtak L. J. et al., 2023, *MNRAS*, 523, 4568
 Harvey D., Massey R., Kitching T., Taylor A., Tittley E., 2015, *Science*, 347, 1462
 Harvey D., Robertson A., Tam S.-I., Jauzac M., Massey R., Rhodes J., McCarthy I. G., 2021, *MNRAS*, 500, 2627
 Heymans C. et al., 2006, *MNRAS*, 368, 1323
 High F. W., Rhodes J., Massey R., Ellis R., 2007, *PASP*, 119, 1295
 Jauzac M. et al., 2016, *MNRAS*, 463, 3876
 Jee M. J., White R. L., Ford H. C., Blakeslee J. P., Illingworth G. D., Coe D. A., Tran K.-V. H., 2005, *ApJ*, 634, 813
 Jee M. J., Mahdavi A., Hoekstra H., Babul A., Dalcanton J. J., Carroll P., Capak P., 2012, *ApJ*, 747, 96
 Jullo E., Kneib J.-P., Limousin M., Elíasdóttir Á., Marshall P. J., Verdugo T., 2007, *New J. Phys.*, 9, 447
 Kaiser N., Squires G., 1993, *ApJ*, 404, 441
 Kaiser N., Squires G., Broadhurst T., 1995, *ApJ*, 449, 460
 Leauthaud A. et al., 2007, *ApJS*, 172, 219
 Lotz J. M. et al., 2017, *ApJ*, 837, 97
 Mahler G. et al., 2018, *MNRAS*, 473, 663
 Massey R. et al., 2007a, *ApJS*, 172, 239
 Massey R. et al., 2007b, *MNRAS*, 376, 13
 Massey R., Kitching T., Richard J., 2010, *Rep. Prog. Phys.*, 73, 086901
 Medezinski E., Umetsu K., Okabe N., Nonino M., Molnar S., Massey R., Dupke R., Merten J., 2016, *ApJ*, 817, 24
 Meneghetti M. et al., 2020, *Science*, 369, 1347
 Meneghetti M. et al., 2023, *A&A*, 678, L2
 Merten J. et al., 2011, *MNRAS*, 417, 333
 Narayan R., Bartelmann M., 1996, preprint(astro-ph/9606001)
 Navarro J. F., Frenk C. S., White S. D. M., 1997, *ApJ*, 490, 493
 Peter A. H. G., Rocha M., Bullock J. S., Kaplinghat M., 2013, *MNRAS*, 430, 105
 Planck Collaboration et al., 2021, *A&A*, 652, C4
 Refregier A., Kacprzak T., Amara A., Bridle S., Rowe B., 2012, *MNRAS*, 425, 1951
 Rhodes J., Refregier A., Groth E. J., 2000, *ApJ*, 536, 79
 Robertson A., Harvey D., Massey R., Eke V., McCarthy I. G., Jauzac M., Li B., Schaye J., 2019, *MNRAS*, 488, 3646
 Sagunski L., Gad-Nasr S., Colquhoun B., Robertson A., Tulin S., 2021, *J. Cosmol. Astropart. Phys.*, 2021, 024
 Schrabback T. et al., 2018, *MNRAS*, 474, 2635
 Sebesta K., Williams L. L. R., Liesenborgs J., Medezinski E., Okabe N., 2019, *MNRAS*, 488, 3251
 Tam S.-I. et al., 2020, *MNRAS*, 496, 4032
 Umetsu K., 2020, *A&AR*, 28, 7
 Weaver J. R. et al., 2024, *ApJS*, 270, 7
 Zhang J., Luo W., Foucaud S., 2015, *J. Cosmol. Astropart. Phys.*, 2015, 024
 Zitrin A. et al., 2010, *MNRAS*, 408, 1916

This paper has been typeset from a $\text{\TeX}/\text{\LaTeX}$ file prepared by the author.